

RESEARCH ARTICLE

10.1002/2017JD027432

Key Points:

- Two-dimensional wavelet analysis is a suitable tool for the scale decomposition of cloud top temperature images
- The combination of temperature and scale information can improve the separation of convective and stratiform cloud parts compared to a temperature-only approach
- Scale detection could help to identify structural changes of mesoscale convective systems at a high spatiotemporal resolution and over climatological time scales

Correspondence to:

C. Klein,  
cornkle@ceh.ac.uk

Citation:

Klein, C., Belušić, D., & Taylor, C. M. (2018). Wavelet scale analysis of mesoscale convective systems for detecting deep convection from infrared imagery. *Journal of Geophysical Research: Atmospheres*, 123, 3035–3050. <https://doi.org/10.1002/2017JD027432>

Received 10 JUL 2017

Accepted 2 MAR 2018

Accepted article online 7 MAR 2018

Published online 25 MAR 2018

# Wavelet Scale Analysis of Mesoscale Convective Systems for Detecting Deep Convection From Infrared Imagery

Cornelia Klein<sup>1</sup> , Danijel Belušić<sup>2</sup> , and Christopher M. Taylor<sup>1,3</sup> 

<sup>1</sup>Centre for Ecology and Hydrology, Wallingford, UK, <sup>2</sup>Swedish Meteorological and Hydrological Institute, Norrköping, Sweden, <sup>3</sup>National Centre for Earth Observation, Wallingford, UK

**Abstract** Mesoscale convective systems (MCSs) are frequently associated with rainfall extremes and are expected to further intensify under global warming. However, despite the significant impact of such extreme events, the dominant processes favoring their occurrence are still under debate. Meteosat geostationary satellites provide unique long-term subhourly records of cloud top temperatures, allowing to track changes in MCS structures that could be linked to rainfall intensification. Focusing on West Africa, we show that Meteosat cloud top temperatures are a useful proxy for rainfall intensities, as derived from snapshots from the Tropical Rainfall Measuring Mission 2A25 product: MCSs larger than 15,000 km<sup>2</sup> at a temperature threshold of −40°C are found to produce 91% of all extreme rainfall occurrences in the study region, with 80% of the storms producing extreme rain when their minimum temperature drops below −80°C. Furthermore, we present a new method based on 2-D continuous wavelet transform to explore the relationship between cloud top temperature and rainfall intensity for subcloud features at different length scales. The method shows great potential for separating convective and stratiform cloud parts when combining information on temperature and scale, improving the common approach of using a temperature threshold only. We find that below −80°C, every fifth pixel is associated with deep convection. This frequency is doubled when looking at subcloud features smaller than 35 km. Scale analysis of subcloud features can thus help to better exploit cloud top temperature data sets, which provide much more spatiotemporal detail of MCS characteristics than available rainfall data sets alone.

## 1. Introduction

The frequency of extreme rainfall events is one of the most relevant climatological aspects for societies worldwide. Torrential rain poses a threat to livelihoods of people, to infrastructure, and to crop yields through erosion, flooding, and the promotion of diseases. Under global warming, rainfall is expected to further intensify due to the increased moisture-holding capacity of a warmer atmosphere (e.g., Allen & Ingram, 2002; Wu et al., 2013). The evolution of convective rainfall is of special interest in this context, since it is not only related to higher local rainfall intensities than stratiform rainfall but also has been found to be highly sensitive to atmospheric warming, significantly exceeding the Clausius-Clapeyron scaling of 7% per degree temperature rise (Berg et al., 2013; Lenderink et al., 2017). Even though deep convection does not cause the majority of extreme rainfall events in all regions of the world, especially where orographic forcing or atmospheric rivers play a strong role for the atmospheric moisture content (e.g., Ai et al., 2016; Liu & Zipser, 2009; Sohn et al., 2013), more than 70% of the global rainfall over land originates from systems with deep convection (Xu & Zipser, 2012).

In West Africa, organized mesoscale convective systems (MCSs) are the dominant rainfall-bearing systems, contributing about 30–80% of the total rainfall during the West African monsoon season over the south-north gradient (Roca et al., 2014). They are commonly defined as large organized thunderstorm complexes of at least 100 km across (Houze, 2004; Laurent et al., 1998; Mohr, 2004). The mechanisms by which MCSs are initiated, organized, and maintained are manifold and range from atmospheric disturbances in the monsoon dynamics and topography (Fink & Reiner, 2003; Mohr & Thorncroft, 2006; Zhang et al., 2016) to surface conditions (Kohler et al., 2010; Taylor et al., 2011).

Most of our current knowledge about MCS circulations and their sensitivities is based on atmospheric models. For example, idealized large-eddy simulations revealed that wind shear can foster convective organization and therefore more intense rainfall (Alfaro & Khairoutdinov, 2015; Froidevaux et al., 2014). Such findings highlighted the importance of storm dynamics for MCS intensification in addition to the

expected thermodynamic sensitivity. However, on the larger scales it remains a challenge to evaluate these mechanisms due to an insufficient representation of MCSs in global circulation models. Convective parameterizations are not yet able to implicitly include the effects of convective organization, leading to large uncertainties in the projections of tropical rainfall extremes (Gorman, 2015).

In addition, observational evidence for supporting modeled findings is needed but often difficult to obtain. In many regions where there is no ground-based radar network and where surface gauges are sparse, observational studies rely on satellite data. Spaceborne rainfall radar data such as from the Tropical Rainfall Measuring Mission (TRMM) provide information intermittently every few days for a given location in West Africa. Complementary microwave data are available every few hours. Both data sets are suitable for building up an understanding of storm characteristics from snapshots taken from different MCSs that occurred over different regions or at different times of day. However, infrequent sampling prohibits more detailed tracking of individual MCS, while the relatively short data set produced by the TRMM satellite limits the possibilities for longer-term trend detection.

On the other hand, geostationary satellites provide long-term subhourly records of cloud top temperatures that provide indirect information on spatial characteristics and on the evolution of rainfall. The Meteosat satellites cover a period of 35 years, allowing analyses on the climatological time scale. This was demonstrated by Taylor et al. (2017), who used the data to reveal a positive trend in MCS intensity in the Sahel for the period 1982–2016. Based on the relationship between colder storm temperatures and more intense rainfall, they identified an increase in the frequency of very cold MCSs with the associated cooling of cloud tops pointing to an intensification of convection. In line with idealized modeling results, they found this trend to be most likely driven by increased wind shear in the region.

In that study, individual storms were analyzed as a single entity neglecting any information on storm structure. Mature MCSs can reach a considerable size (more than 100,000 km<sup>2</sup>) of which only a small areal fraction is producing very intense rainfall. To be able to pinpoint these intensely precipitating convective cores becomes of importance if trends in extreme rainfall are to be evaluated for specific locations. Local-scale vegetation patterns or land use changes have the potential to directly modify rainfall amounts (Hartley et al., 2016; Klein et al., 2017; Lauwaet et al., 2009). The associated change in MCS structure can only be detected and related to these surface properties if the location of the convective area within the MCS is known.

A common way for identifying intensely precipitating convective areas from infrared brightness temperature images is to apply a temperature threshold, assuming that the coldest cloud top temperatures are associated with highest vertical velocities. Since the ideal temperature threshold varies, this method must be carefully adapted to different climatic regimes. Nevertheless, satellite infrared images are frequently used to evaluate global and regional characteristics of deep convection (e.g., Adler & Negri, 1988; Fiolleau & Roca, 2013; Goldenberg et al., 1990) and numerous rainfall products rely on indirect retrievals of rainfall rates from cloud top temperatures (Ashouri et al., 2015; Joyce & Arkin, 1997; Wolters & Roebeling, 2011). Initiatives like the “Tropical Applications of Meteorology using Satellite data and ground-based observations” (Maidment et al., 2014) derive optimized regional temperature thresholds based on rain gauge records to identify precipitating clouds as well as to calibrate pixel-based rainfall amounts. A remaining problem with such rainfall retrieval algorithms is their limited ability to distinguish convective regions from cirrus clouds or cold stratiform anvils. Their suitable calibration therefore remains a challenge and might require compromise. For example, the focus of Tropical Applications of Meteorology using Satellite data and ground-based observations on drought monitoring necessitates a high sensitivity to small rainfall amounts, which causes an underestimation of intense rainfall (Maidment et al., 2017).

Other, more complex rainfall retrieval algorithms employ neural networks to additionally classify cloud structures from thermal infrared images (e.g., Ashouri et al., 2015; Mahrooghy et al., 2012). Information on the cloud texture and its temporal evolution improve the discrimination of convective, stratiform, and nonraining cloud parts. This is because these cloud parts exhibit systematic differences not only in their vertical extent but also in their horizontal structure. This was already shown by Vicente et al. (1998), who identified local temperature gradients within kernels of 20 km<sup>2</sup> in order to discriminate rain/no-rain areas for the application of a cloud top temperature-precipitation regression relationship. They argued that pixels above the average cloud top surface height should be associated with active convection and precipitation beneath. They

found that weak cloud top temperature gradients are indeed helpful for screening out nonraining anvil cirrus developing during the mature stage of storms. Currently existing techniques for the detection of convective cloud areas from infrared imagery with little dependence on temperature thresholds, such as the window-texture method (Bedka & Khlopenkov, 2016) or the brightness temperature method (Ai et al., 2017), were explicitly developed for the detection of overshooting tops (OTs), that is, cloud areas where strong vertical updrafts penetrate into the tropopause. OTs were found to often be associated with severe weather and intense convective rainfall and hence are a useful indicator for potentially destructive storms in operational applications (Dworak et al., 2012). Both methods therefore aim at a high predictive performance for individual storms. In the case of the window-texture method, additional input from numerical weather prediction models and Moderate Resolution Imaging Spectroradiometer observations are integrated in the workflow.

In this study, we do not specifically focus on detecting OTs but are evaluating the general usefulness of length scale information for the identification of intensely precipitating cloud parts. We further explore the relationship between temperature gradients and rainfall via a scale analysis of the cloud structure applied to West African MCSs. While the area of a convective core in a big storm can be extensive, it is of smaller scale than the area of the stratiform cloud shield and is interspersed with individual intensive updrafts. This makes the convective area more heterogeneous (i.e., featuring smaller scales), than areas with stratiform rainfall where the cloud is dispersing and vertical velocities are low (Houze, 2004). Different from current applications of texture scanning with neural networks, our aim is not a pixel-based rainfall retrieval, which necessitates strict testing of forecast skill and temporal rainfall aggregation for improved accuracy. Instead, we assess whether the length scales of subcloud features (SCFs) have the potential to give instantaneous information on the localization of intensely precipitating convective cloud areas. A probabilistic link between SCF length scales and the occurrence of convective rainfall could facilitate the detection of structural changes in MCSs, which would be a valuable research tool for understanding dynamics within MCSs.

Following the findings of Taylor et al. (2017), the identification of such changes over climatological time scales could be a useful tool for interpreting existing long-term trends in cloud top temperature. At the same time, the analysis of convective-scale features may provide important evidence on how land surface properties influence rainfall within organized systems (e.g., Taylor & Lebel, 1998). For this, we developed a method for scale decomposition of MCS cloud top temperatures into SCFs with continuous wavelets. The identified SCFs are then linked to TRMM rainfall fields to evaluate the added value of that length scale information. First, results for the relationship between SCFs and rainfall characteristics are presented and methodological options are discussed.

## 2. Region and Data

### 2.1. Cloud Top Temperature and Rainfall Data

The study encompasses the whole West African region (Figure 1) and focuses on the monsoon months June–September, when MCSs are most frequent.

We use thermal infrared brightness temperature data (10.8  $\mu\text{m}$ , channel 9) from the Spinning Enhanced Visible and Infrared Imager of the geostationary Meteosat Second Generation (MSG) satellites. The data are freely available from the EUMETSAT website (<http://www.eumetsat.int>) every 15 min at an approximate spatial resolution of 3 km over West Africa. We used lookup tables provided by EUMETSAT to convert the data from effective radiances to brightness temperatures, hereafter referred to as “cloud top temperatures.” These cloud top temperatures were then filtered for two temperature thresholds,  $< -10^\circ\text{C}$  and  $-40^\circ\text{C}$ , with contiguous pixel areas defining individual clouds. Only clouds of at least 350  $\text{km}^2$  were kept for both thresholds.

In order to obtain information on surface rainfall characteristics at a relatively high spatial resolution, we use the TRMM product 2A25 (Tropical Rainfall Measuring Mission, 2011). This rainfall radar product provides snapshots of surface rainfall rates from 2 to 4 overpasses per day across our domain at a resolution of about 5 km. In the absence of surface radar or dense gauge observations, this provides the best observation of spatial variations in precipitation over West Africa. Equally, it has already been used for analyzing life cycles and the vertical structure of African MCSs (Futyan & Del Genio, 2007; Geerts & Dejene, 2005). Specifically for West Africa, it has been, among others, applied as a reference for other rainfall products (Wolters & Roebeling, 2011), for compiling a climatology of MCS rainfall characteristics (Guy & Rutledge, 2012) and for identifying

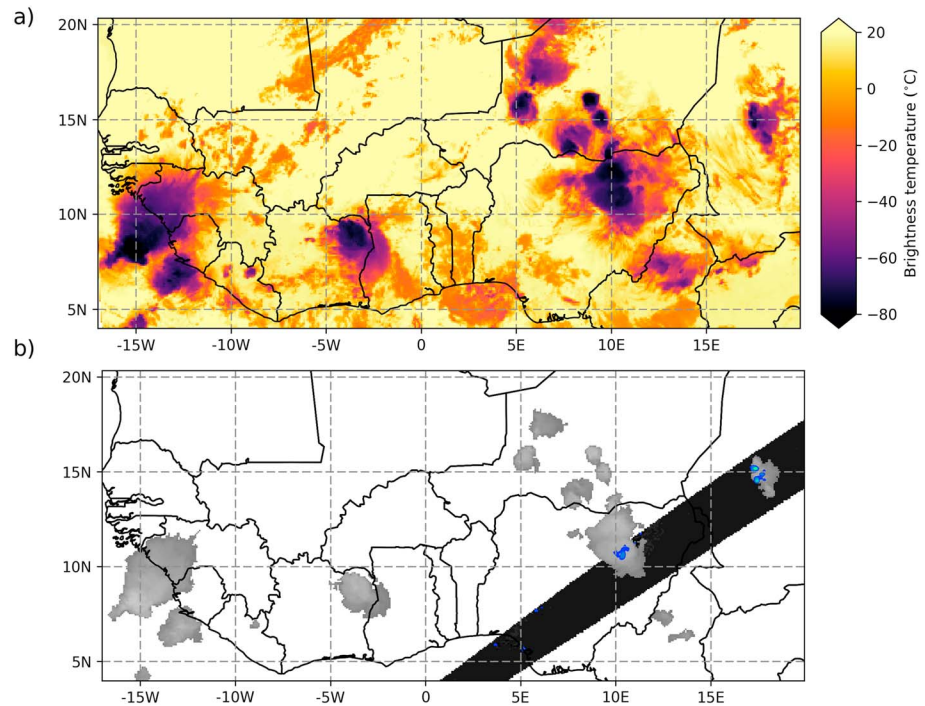


**Figure 1.** Study domain showing an example for (a) the infrared temperature data derived from Meteosat Second Generation and (b) identified clouds at a temperature threshold of  $-40^{\circ}\text{C}$  with a minimum area threshold of  $350\text{ km}^2$  (gray) and the overlapping Tropical Rainfall Measuring Mission swath (black) on the  $5\text{ km}$  grid. Tropical Rainfall Measuring Mission rainfall is indicated in blue.

different rain types within MCSs (Schumacher & Houze, 2006). Validation studies report a likely underestimation of intense convective rainfall rates of the product but overall find a realistic spatial rainfall distribution, which allows to distinguish convective and stratiform storm areas (Iguchi et al., 2009; Rasmussen et al., 2013).

An individual TRMM swath is approximately  $250\text{ km}$  wide (Figure 1b) and covers the same point on the surface at a different local time every one to 4 days (23–46 days for a return at the same local time). In addition, the data set provides a classification flag for convective rainfall, as diagnosed from the bright band vertical and horizontal structure (Awaka et al., 1997). This flag is used in combination with a minimum rainfall threshold of  $8\text{ mm h}^{-1}$  to define convective rainfall pixels in TRMM. For all analyses presented here, the two data sets were regridded onto a common grid of  $5\text{ km}$  resolution for 2004 to 2014, the time period overlapping with TRMM (cf. Figure 1a). We use temperature lapse rates from ERA-Interim (Dee et al., 2011) to correct for parallax due to the difference in viewing angles of the two satellites (Mahani et al., 2000). For each TRMM overpass, we identified MSG cloud structures containing at least three valid TRMM pixels. The MSG image used was selected to be coincident or within a maximum of 30 min ahead of the TRMM overpass. In the example shown (Figure 1b), the TRMM overpass samples two distinct cold clouds.

### 3. Bulk-Relationship of Cloud Top Temperatures and Extreme Rainfall

Before examining relationships between SCFs and associated local rainfall, following Taylor et al. (2017), we consider how the probability of extreme rain varies with the minimum temperature and size of cloud systems. For exploring the general relationship of cloud top temperatures and rainfall at the cloud scale, we first identified the minimum temperature and maximum rainfall within 13,845 clouds of a size of at least  $350\text{ km}^2$  at a temperature threshold of  $-10^{\circ}\text{C}$ . These size and temperature thresholds include smaller clouds that would not be characterized as MCSs, but they allow us to evaluate their contribution to occurrences of extreme rainfall. In the following, we define extreme rainfall as rain exceeding  $30\text{ mm h}^{-1}$ , which corresponds to the 99th percentile of all rainy TRMM pixels ( $>0.1\text{ mm h}^{-1}$ ) within contiguous clouds below  $-10^{\circ}\text{C}$ .

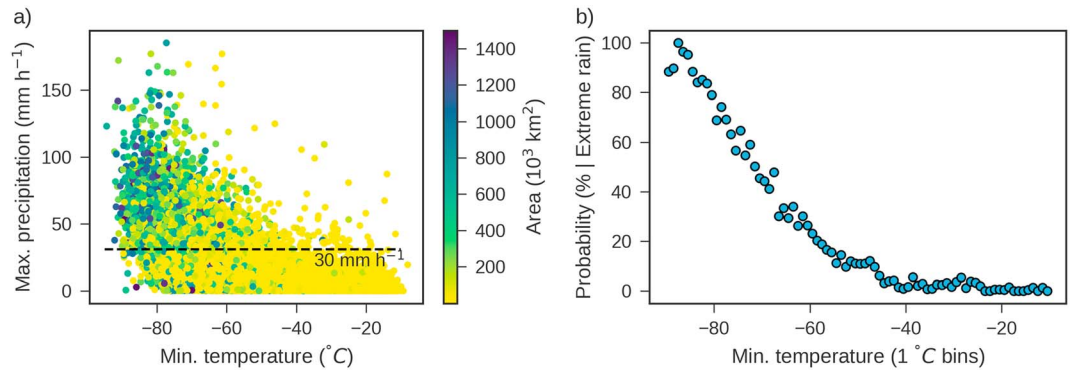


**Figure 2.** Relationship of June–September 2004–2014 minimum cloud top temperature and maximum precipitation within contiguous clouds larger than  $350 \text{ km}^2$  above a temperature threshold of  $-10^\circ\text{C}$ . Scatter plots of minimum temperature versus (a) maximum precipitation and (b) probability for rainfall above  $30 \text{ mm h}^{-1}$  (99th percentile) per cloud. The coloring in (a) indicates the total cloud area.

Figure 2a illustrates the tendency for maximum rainfall intensity per storm to increase with decreasing minimum temperature, that is, a higher cloud top, as expected. In 86% of the cases where clouds produce any extreme rain (points above the dashed line), they exhibit a minimum temperature below  $-60^\circ\text{C}$ . Binning each cloud according to its minimum temperature (Figure 2b), we found that 83.7% of the storms that reach a minimum temperature below  $-80^\circ\text{C}$  are associated with extreme rain. This probability drops to 1.5% for clouds with a minimum temperature warmer than  $-40^\circ\text{C}$  (Figure 2b). For all following analyses, we therefore apply a temperature threshold of  $< -40^\circ\text{C}$  in order to exclude cloud areas that are unlikely to produce any extreme rainfall.

Alongside cloud top temperature, cloud size is expected to affect the maximum rainfall amount. As visible from Figure 2a, large clouds are much more likely to produce extreme precipitation than the more numerous small clouds. We quantify this effect in Figure 3 by applying increasing cloud area thresholds. The blue dotted curve shows only a slight drop in the absolute number of extreme rainfall pixels when smaller clouds are excluded, while there is a sharp decrease for very large clouds. Using a threshold of  $-40^\circ\text{C}$ , 91% of the absolute number of extreme rainfall pixels occur in only 33% of the clouds, that is, clouds larger than  $15,000 \text{ km}^2$ . This area threshold also increases the fraction of rainy clouds from 77% to 91% (Table 1). However, it should be noted that while the threshold results in a considerable decrease in the number of clouds (67%), the decrease in cloud area is only 13%. This illustrates that very large cloud clusters generally dominate the cold

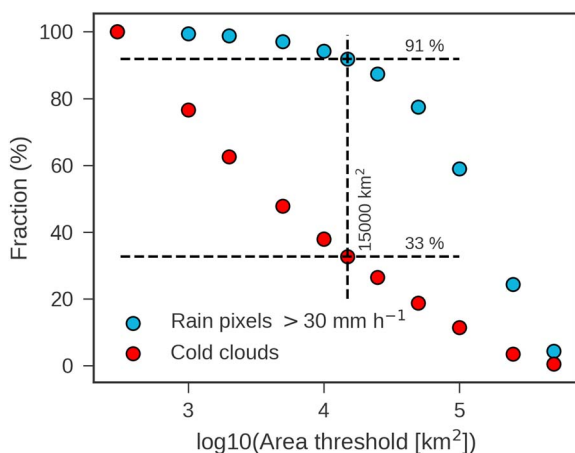


**Figure 3.** Cumulative fraction of retained extreme rainfall pixels (blue) and cold clouds (red) for increasing area thresholds ( $\text{km}^2$ , log scale) with respect to the total number of extreme rainfall pixels and the total number of cold clouds, respectively. Contiguous cold clouds are defined with a temperature threshold of  $-40^\circ\text{C}$ .

cloud cover over the study region, which is in line with Mathon et al. (2002). By combining Meteosat data with rain gauges, they found mature organized MCSs to represent 80% of the cloud cover below  $-40^\circ\text{C}$  while only contributing 18% in cloud number.

Our results confirm that large, cold MCSs are responsible for the vast majority of extreme rainfall in West Africa during the monsoon, as was also shown by Taylor et al. (2017) for a Sahelian domain ( $11\text{--}18^\circ\text{N}$ ). Cloud top temperature proves to be a useful characteristic for determining the probability of a storm to produce intense rain in a bulk approach. The question we now consider is whether additional information about intense rainfall can be obtained from subcloud temperature features.

#### 4. Wavelet Analysis

We now use a 2-D continuous wavelet transform (CWT) approach to decompose the MSG cloud top temperatures into a wavelet power spectrum representing scales between 15 and 180 km. The goal is to identify contiguous subcloud features that are characterized by a temperature gradient at their edges and a homogeneous interior relative to the respective scale.

**Table 1**

Statistics of Detected Cold Clouds With TRMM/MSG Overlap Between June and September 2004–2014 at a Temperature Threshold of  $-40^{\circ}\text{C}$

	Clouds > 350 km <sup>2</sup>	Clouds (MCSs) > 15,000 km <sup>2</sup>	Subcloud features
Cloud number	13,845	4,530	4,011
TRMM/MSG overlapping cloud area (10 <sup>6</sup> km <sup>2</sup> )	169	147	60
Rainy cloud fraction (%)	76.8	91.3	92.1
Rainy pixel fraction (%)	27.7	28.5	40.3
Conditional mean rainfall (mm h <sup>-1</sup> )	5.86	5.87	6.69
Convective rain pixel fraction $\frac{\text{Pixel}_{\text{convective}}}{n}$ (%)	3.8	4.1	7.3
Extreme rain pixel fraction $\frac{\text{Pixel}_{\text{extreme}}}{n}$ (%)	0.5	0.6	1.1
Fraction of excluded extreme pixels (%)	/	8.7	18.2

*Note.* All measures consider the Tropical Rainfall Measuring Mission (TRMM)/Meteosat Second Generation (MSG) overlapping cloud areas only. Pixels with rain  $>1 \text{ mm h}^{-1}$  are defined as rainy pixels. A cloud with at least one rainy pixel is counted as rainy. Mean rainfall values are for rainy pixels only.  $N$  is the total number of overlapping pixels, including those with zero rainfall. The threshold for extreme rainfall is  $30 \text{ mm h}^{-1}$ . The reference for the fraction of excluded extreme rainfall pixels due to respective filtering is the number of extreme rainfall pixels found in clouds  $>350 \text{ km}^2$ . Refer to section 4 for the detailed definition of subcloud features. MCSs = mesoscale convective systems.

The 2-D CWT is the method of choice because it is most commonly used for feature detection in images (e.g., Antoine, 2004). In atmospheric science, both continuous and discrete 2-D wavelet analyses have been considerably less used than their 1-D counterparts. Raut et al. (2009) used 2-D discrete wavelet transform to detect convective clouds in thermal imagery as features smaller than 40 km, and a few studies have used it for spatial verification of numerical weather prediction models (Yano & Jakubiak, 2016; Weniger et al., 2017, and references therein). Wang and Lu (2010) introduced and illustrated several examples of meteorological applications of 2-D CWT.

Two-dimensional CWT is a straightforward extension of one-dimensional CWT (e.g., Torrence & Compo, 1998) to two spatial dimensions. The 2-D CWT can in general be used to detect directionally oriented features, provided an anisotropic wavelet function is used (e.g., Weniger et al., 2017). For simplicity, we here choose an isotropic wavelet function and hence nondirectional 2-D CWT. Following the notation from Wang and Lu (2010), the nondirectional 2-D CWT of a two-dimensional signal function  $f \in L^2(R^2)$  can be expressed as

$$(Wf)(a, \mathbf{b}) = \int_{R^2} f(\mathbf{x}) \overline{\psi}_{a,\mathbf{b}}(\mathbf{x}) d\mathbf{x},$$

$$\psi_{a,\mathbf{b}}(\mathbf{x}) = a^{-1} \psi\left(\frac{\mathbf{x}-\mathbf{b}}{a}\right),$$

where  $a$  is the wavelet scaling parameter,  $\mathbf{b} \in R^2$  is the wavelet position (shifting) vector,  $\psi$  is the wavelet mother function,  $\mathbf{x}$  is the variable in two-dimensional vector space with the components  $(x, y)$ , and the overbar indicates complex conjugate of a function. Note that the actual computations are performed in Fourier space due to higher efficiency (e.g., Torrence & Compo, 1998; Wang & Lu, 2010). The wavelet power spectrum is defined as  $|(Wf)(a, \mathbf{b})|^2$ . High power values at a certain length scale indicate features with a relatively large amplitude and high similarity to the shape of the mother wavelet at that length scale.

Based on the results from the bulk analysis of clouds, this length scale decomposition is conducted only for the 4,530 contiguous clouds that exhibit a minimum area of 15,000 km<sup>2</sup> at a temperature threshold of  $-40^{\circ}\text{C}$  (cf. Table 1). This means that we are focusing on well-organized, cold MCSs during their mature stage (Futyan & Del Genio, 2007). This stage is typically reached several hours after convective initiation and is characterized by an established mesoscale circulation throughout the system (e.g., Houze, 2004). Within a mature MCS, several new, heavily precipitating convective cells coexist with a large anvil region with light stratiform rainfall as well as with nonprecipitating anvil regions that stem from former convective cores. Furthermore, given the chosen temperature and area threshold, our sampling inevitably includes stratiform anvils of decaying MCSs without any active convection.

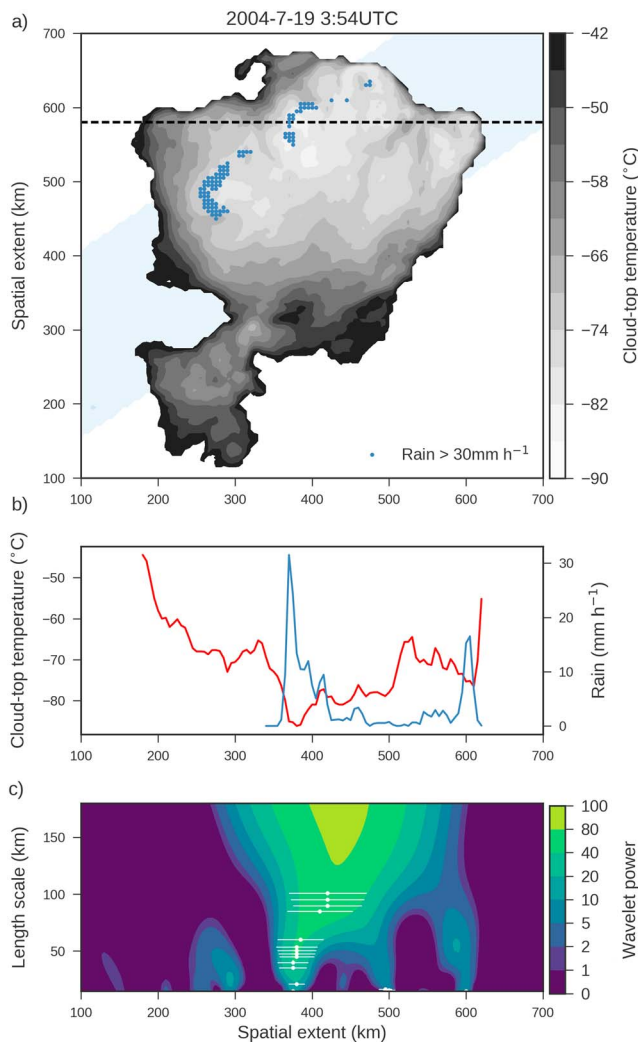


**Figure 4.** Illustration of the wavelet scale decomposition for a single mesoscale convective system. (a) Cloud top temperatures (gray shading) and TRMM overpass (light blue). The blue lines show the edge of the Tropical Rainfall Measuring Mission swath with blue dots indicating locations of extreme rainfall. The black dashed line marks the position of the cross section for (b) temperature (red) and rainfall (blue) and (c) wavelet power values for all length scales. White circles and whiskers in (c) indicate local wavelet power maxima and the extent of the SCF.

Following Wang and Lu (2010), the applied wavelet mother function ( $\psi$ ) is the Laplacian of the 2-D Gaussian (LoG) function, also known as the Mexican Hat or Marr wavelet:

$$\psi(\mathbf{x}) = (2 - |\mathbf{x}|^2)e^{-\frac{|\mathbf{x}|^2}{2}}.$$

The LoG is isotropic and is a widely used filter for the detection of “blobs” and edges in images (e.g., Marr & Hildreth, 1980). With respect to cloud structures, the LoG will identify sharp changes of cloud top temperatures, either at the edges of the clouds or for cold features within the clouds. Since we are only interested in the latter, edge effects were reduced by setting the background temperature (the noncloud area) to the 50th percentile temperature of each individual MCS. The cloud edges were then smoothed with a Gaussian filter within a  $3 \times 3$  pixel kernel before applying the wavelet transform.

Figure 4 illustrates the wavelet scale decomposition for a west-east transect through an MCS that produced extreme rainfall, according to TRMM (Figure 4a). The transect of cloud top temperature and rainfall shows extreme rainfall coinciding with lowest temperatures at the location between 360 km and 420 km (Figure 4b). At the same time, we detect high wavelet power values down to the smallest length scales in these areas (Figure 4c). Local power maxima are depicted in white in Figure 4c and are identified per length scale in a moving window within a 2-D footprint of  $30 \times 30 \text{ km}^2$ . For each individual cloud, only identified maxima surpassing the 90th percentile of occurring power values within the respective scale and above a minimum value of  $\sqrt{\text{scale}}$  are considered significant. The scale-dependant minimum threshold favors the identification of small SCFs but at the same time excludes those identified in predominantly homogeneous clouds.

The extracted power maxima represent the center points of SCFs at the respective scale with a radius of  $\frac{\text{scale}}{2}$  (cf. whiskers). Since Figure 4c depicts only power maxima situated along the transect, they are only visible up to 100 km before shifting toward the cloud center for bigger scales.

The wavelet power values (and therefore power maxima) do not depend on absolute temperature values but solely on the temperature gradient between feature and background. Warm SCFs could theoretically exhibit a similar wavelet signal as cold SCFs if they were confined by a temperature gradient of a similar margin, rendering the wavelet signal dependant on the relative temperature structure only.

#### 4.1. Temperature and Rainfall Structures in the Vicinity of Local Power Maxima

We now consider the performance of the wavelet approach in identifying extreme rain across our data set of 4,011 clouds within which significant SCFs were detected (cf. cloud number in Table 1). Figure 5 shows a composite of cloud top temperatures and associated likelihood of extreme rainfall for different length scale ranges. The composites are centered on the wavelet power maximum of each SCF (cf. Figure 4c, white dots), that is, on the center of a bump at the cloud top of the respective scale within a window of  $200 \text{ km} \times 200 \text{ km}$ .

Based on the composite average, the wavelet decomposition picks up cold circular temperature structures with a diameter corresponding to the expected length scales. It should be noted that this gives no information on the shape of individual SCFs, which are naturally rarely circular. The composite circular feature is produced by averaging noncircular temperature structures randomly oriented in space.

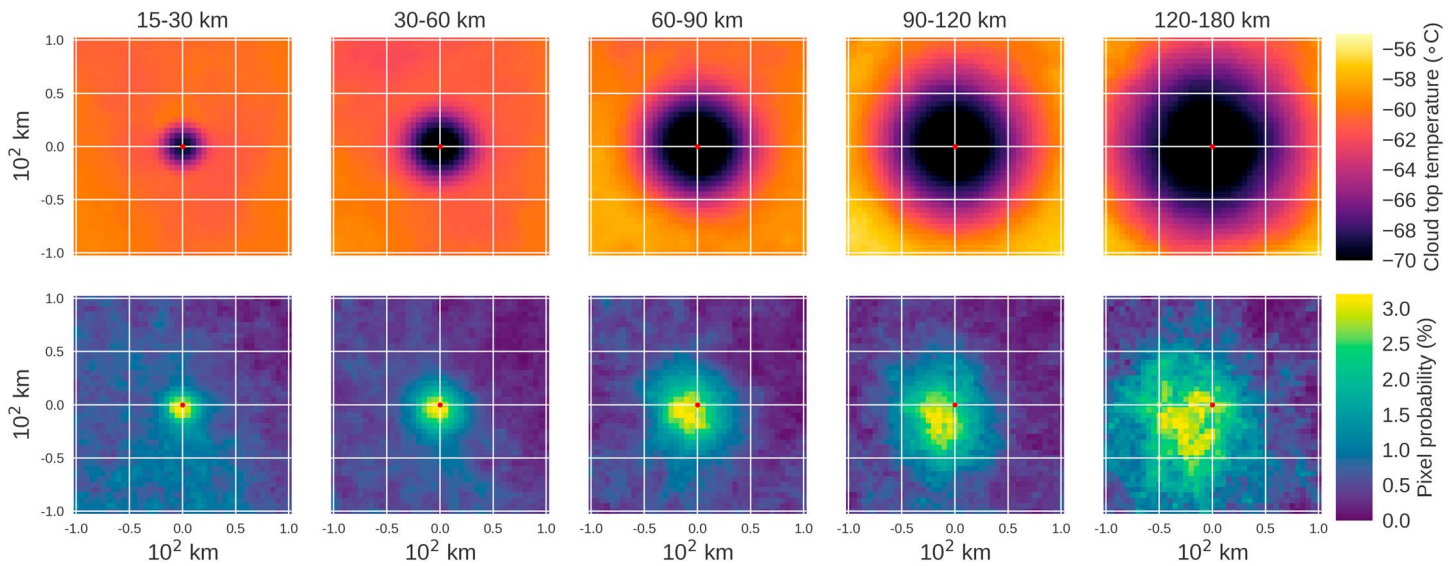


**Figure 5.** Composites centered on power maxima for SCFs at different scale ranges for (top row) the associated cloud top temperatures and (bottom row) the probability for extreme rain ( $> 30 \text{ mm h}^{-1}$ ) at location  $\Delta x, \Delta y$  from the composite center (red dot). The pixel probability is defined as the fraction of extreme rain with respect to the number of valid pixels at each location.

The lower panel of Figure 5 illustrates that it is indeed possible to relate the spatial distribution of extreme rain to substructures of the cloud in a statistical sense: there is a preference for extreme rainfall in the vicinity of the center of SCFs of all scales. Interestingly, for SCFs with a diameter above 60 km, highest probabilities for extreme rain become displaced to the southwest of the SCF center point, indicating regions of convective rainfall at the front of the storms. This southwestward displacement is caused by a propagation tendency in the southwest direction of many MCSs, antiparallel to the monsoon winds, the direction of strongest low-level moisture convergence (Corfidi, 2003; Hodges & Thorncroft, 1997).

#### 4.2. Dominant-Scale Detection Versus Small-Scale Detection

For any point within a storm, the wavelet scale decomposition identifies multiple length scales that might be considered significant depending on the application. Consequently, there are different approaches for defining a single length scale that a specific region of the cloud belongs to, given the maxima within the wavelet power spectrum. One option is to further filter the local power maxima in the scale dimension ( $x, y, \text{scale}$ ), hence identifying the scale at which an SCF possesses the steepest temperature gradient at its edges. This dominant-scale detection is suitable for measuring the overall extent of cold areas within an MCS. These often reach scales of 50 km or more. However, with this method there can be a loss of information on embedded smaller-scale perturbations where these do not exhibit a strong enough temperature decrease with respect to the often already very low background temperature.

Instead, here, we are specifically interested in the localization of small-scale features at the cloud top. The assumption is that relatively small “bumps” could indicate convective cores, even if the temperature gradient with respect to their immediate surroundings is weaker than for the bigger cloud shield they are embedded in. Analyses of the internal structure of MCSs based on rain radar have shown that convective rain areas contain strong peaks in precipitation intensity at a horizontal scale of 1–10 km, indicating single convective cells, which organize into bigger clusters or a band of convection within the MCSs (e.g., Cheng & Houze, 1979; Houze et al., 2015; Parker & Johnson, 2000). If these confined areas of peak precipitation are collocated with strong vertical updrafts, we should see a SCF at the cloud top of a comparable or somewhat larger scale (since the cloud bump disperses horizontally) associated with that updraft.

We therefore employ a small-scale detection method that identifies the local power maxima of the 2-D wavelet power spectrum for each individual scale in the space dimensions ( $x, y$ ) only, as was presented in Figure 4c for one transect. For simplicity, we then define each SCF area to be encompassed by circles with the radius  $\frac{\text{scale}}{2}$ . Starting at the maximum scale of 180 km, each pixel in these circles is assigned the value of

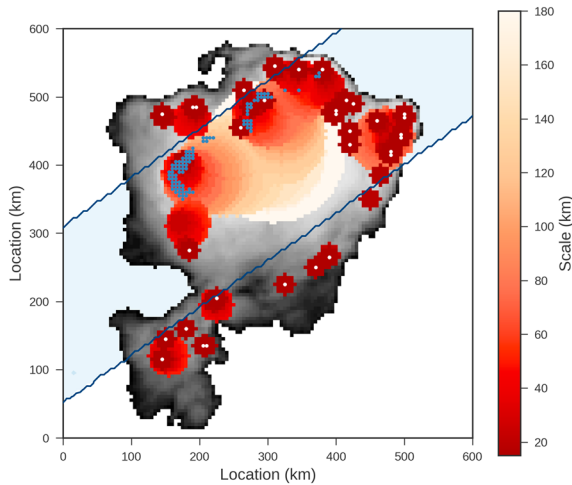


**Figure 6.** Illustration of the small-scale detection method for the same mesoscale convective system as in Figure 4 with circles indicating the assigned scales derived from local power maxima of the wavelet scale decomposition. White dots indicate the wavelet power maxima (circle center points) for the smallest scale of 15 km. Regions of the mesoscale convective system without any scale assignment are ignored. Blue lines show the edge of the Tropical Rainfall Measuring Mission swath with blue dots indicating extreme rain.

that scale. The procedure is repeated for gradually smaller scales, following the rule that signals for smaller scales overwrite larger scales. The resulting image provides a map depicting the smallest length scales associated with SCFs across the cloud. Figure 6 illustrates the resulting image for one individual MCS with overlaid scale identification: light colors indicate larger-scale SCFs in areas with a homogeneous cloud top, while dark red circles mark the smallest wavelet-identified SCFs where “bumps” that could indicate convection are apparent. The SCFs can then be mapped back onto the cloud top temperature image and TRMM overpasses. This allows us to assign temperature and rainfall characteristics to SCFs at different scales. For example, extreme rainfall pixels marked in Figure 6 are mostly collocated with SCFs of scales smaller than 40 km. Note that only SCF pixels with an overlap with the respective TRMM swath (indicated by blue lines in the example in Figure 6) are considered.

The rationale for favoring the smallest scale with a signal is based on the idea that existing bigger scales represent cloud levels with larger horizontal extent, which are lower and warmer than towering smaller scales on top. Small-scale features should in many cases be associated with locally higher vertical velocities with respect to their surroundings, which would be characteristic for convective updrafts. Consequently, in the case of a scale overlap, we assign the temperature and rainfall within the respective SCF to the smallest occurring scale, avoiding

double assignment. This approach also means that the cloud areas left assigned to large scales should be relatively homogeneous, without considerable small-scale structure. When applied across the data set of MCSs  $>15,000 \text{ km}^2$  at  $-40^\circ\text{C}$ , this method excludes about 60% of the overlapping TRMM/MSG pixels in MCSs while still retaining 90% of the number of extreme rain occurrences. At the same time, the fraction of rainy pixels ( $\geq 1 \text{ mm h}^{-1}$ ) increases from 28.5% to 40.3% (Table 1).

The frequency distributions of individual pixel temperatures within SCFs derived with this method for three length scale ranges are shown in Figure 7a. The ranges are chosen to ensure a similar sample size in terms of valid overlapping temperature/rainfall pixels associated with the SCFs (approximately one million valid pixels per length scale range). Comparing the different scales, SCFs above 90 km mainly pick up the edges and homogeneous parts of the MCSs, causing their temperature distribution to be shifted toward warmer pixels at lower altitudes. On the other hand, the smallest scales also show a slightly warmer distribution than intermediate (35–90 km) scales. This indicates that small bumps in the cloud top are often found in warm as well

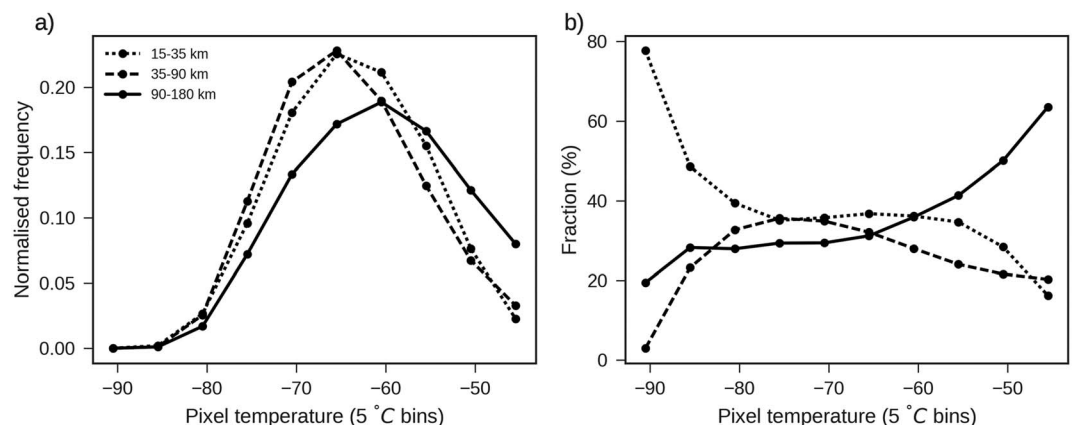


**Figure 7.** Temperature distribution for pixels within subcloud features identified via small-scale detection for different length scale ranges. (a) Normalized frequency and (b) the fraction of pixels per temperature bin.

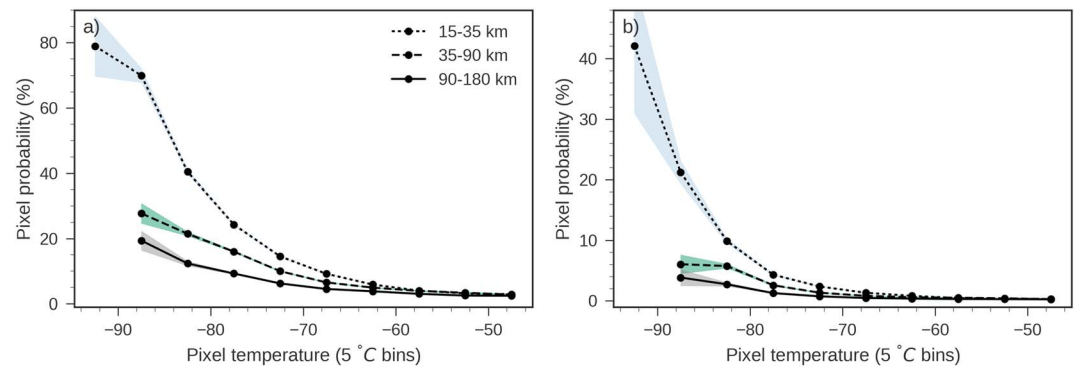


**Figure 8.** Dependence of the probability for intense rainfall on cloud top temperature and length scale. Probability per pixel with respect to the number of valid pixels for (a) convective rainfall identified from the Tropical Rainfall Measuring Mission convective rainfall flag with a minimum threshold of  $8 \text{ mm h}^{-1}$  and (b) extreme rainfall ( $> 30 \text{ mm h}^{-1}$ ). Uncertainty ranges indicate the 95% binomial confidence interval depending on the sample size. Points indicate the center point of each temperature bin.

(Figure 7b), SCFs between 15 and 35 km contribute the biggest share (40%) of cold pixels below  $-80^\circ\text{C}$ . At the other end of the temperature scale, 55% of all pixels associated with an SCF with an average temperature above  $-50^\circ\text{C}$  belong to SCFs larger than 90 km. Given the established relationship of lower temperatures with more intense rainfall (Figure 2a), the typically higher temperatures at larger scales suggest lower probabilities for intense rain associated with these MCS regions.

## 5. Rainfall Characteristics Associated With Subcloud Features

### 5.1. Probability for Convective Rainfall

We now use the assigned scales to separate different cloud areas in order to evaluate their respective probabilities for convective and extreme rain. The pixel probabilities in Figure 8a are computed from cloud top temperature pixels within SCFs that overlap with valid TRMM pixels and are averaged over temperature and scale bins. Overlaps with zero rainfall are explicitly included in all probability calculations to take into account “false alarm” cases.

For the whole temperature range, SCFs smaller than 35 km show higher probabilities for convective rain than those associated with larger scales. This suggests that actively convective parts of MCSs indeed produce small-scale structures via vigorous vertical updrafts, which can be detected with the scale decomposition subcloud features less than 35 km are closest to the scales at which convective cells and associated contiguous intense rainfall occurs within the MCSs (cf. section 4.2). On the other hand, larger scales are mostly identified in relatively homogeneous parts of the MCS where stratiform rainfall can be expected. Correspondingly, temperatures below  $-90^\circ\text{C}$ , which indicate deep convection in 79% of the cases, are only present for scales below 35 km. Below  $-80^\circ\text{C}$ , at least every third pixel is associated with convective rain for scales smaller than 35 km. The probability for the occurrence of extreme rain follows approximately the same relationships with scale and temperature (Figure 8b). Below  $-60^\circ\text{C}$ , the 35 km scale threshold increases the probability for extreme rain by a factor between 1.5 and 3.5 compared to the larger scales.

### 5.2. Temperature Threshold Versus Added Scale Information

Given the promising results of using the small-scale detection to filter cloud parts that are more likely to produce intense rain, we now want to evaluate whether this approach adds any value compared to the common method of applying a temperature threshold (e.g., Maidment et al., 2014). While temperature is the most valuable indicator for cloud top height and therefore convective activity, the ideal threshold for identifying the coldest cloud tops varies with climate region and season. In addition, a temperature threshold might not be sufficient for excluding cold stratiform cloud parts. The length scale of SCFs on the other hand is independent from absolute temperatures and therefore provides additional information on the type of feature that is identified.

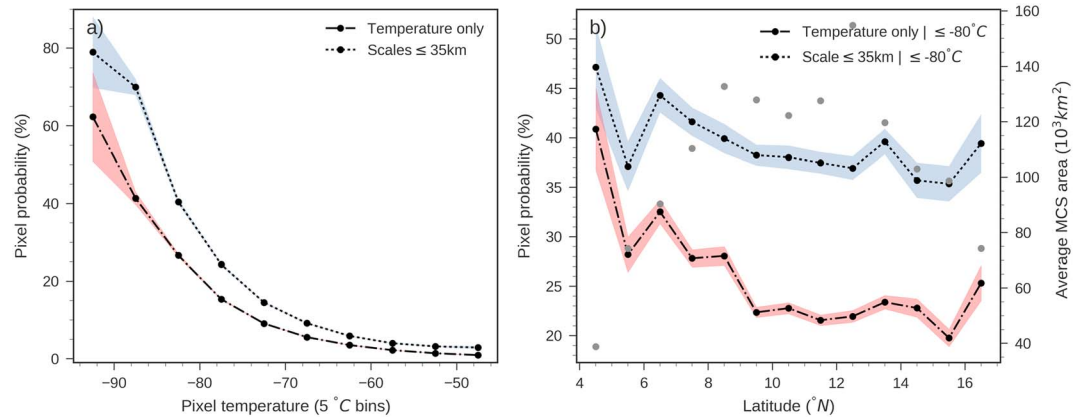


**Figure 9.** Comparison of the probability for convective rainfall derived by using a temperature threshold only (red) and by additionally restricting the analyzed cloud areas to scales  $\leq 35$  km (blue). (a) Pixel probability as in Figure 8a. (b) Meridional cross section of average pixel probabilities between 17°W and 30°E with a temperature threshold of  $-80^{\circ}\text{C}$  and average mesoscale convective system area based on all storms below  $-40^{\circ}\text{C}$  (gray dots).

We compare the small-scale detection method to a simple temperature-based approach where no SCFs are defined. The entire overlapping area between TRMM and MSG from 4,011 MCSs is considered to derive the relationship between cloud top temperature and the probability for convective rain. Figure 9a shows that the additional application of a small-scale threshold increases the pixel probability for convective rainfall for all temperatures. The two methods appear to converge for those very cold temperatures (below  $-90^{\circ}\text{C}$ ) that are only reached by small scales in the first place. Considering all SCFs smaller than 35 km and below  $-80^{\circ}\text{C}$ , 40% of the rainfall pixels are marked as convective by the TRMM rainfall flag, while this is true for only 21% when only considering temperature. This confirms that scale information can be a useful addition to information on cloud top temperature.

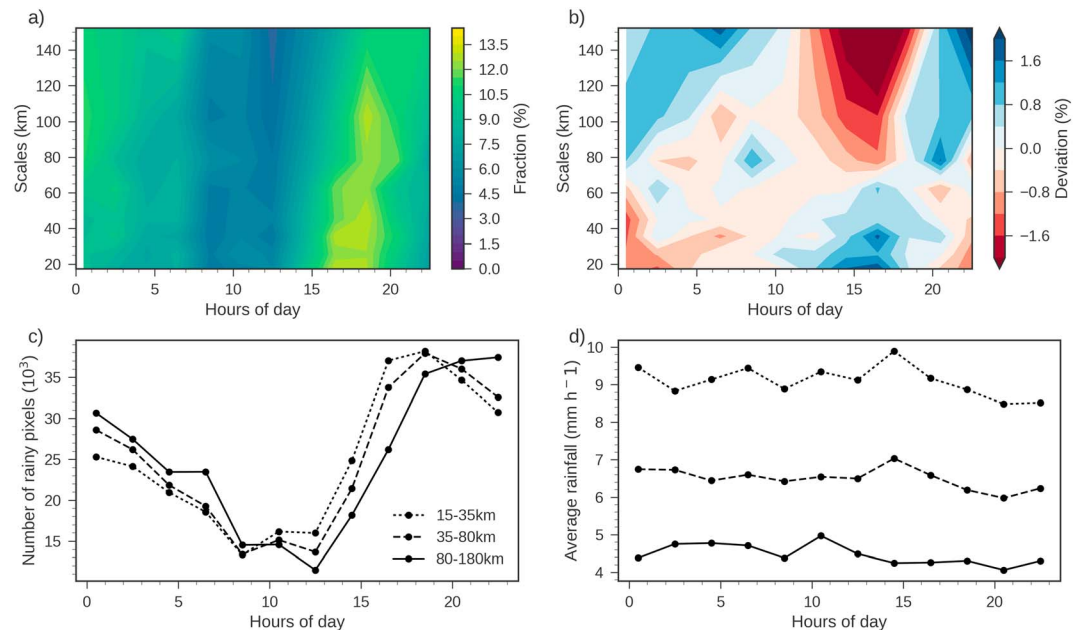


**Figure 10.** The diurnal cycle for 2-hourly bins of subcloud feature length scales and associated precipitation. (a) Relative precipitation contribution per scale over the diurnal cycle and (b) deviation from the mean relative precipitation distribution per scale. In (a), the sum over the diurnal cycle is 100% for every individual scale. In (b), the sum over all scales is 0% for every 2 h. (c and d) The number of rainy pixels ( $>1 \text{ mm h}^{-1}$ ) and average rainfall for given scale ranges, respectively. The scale ranges in (c) and (d) were chosen to contain a similar number of rainy pixels.

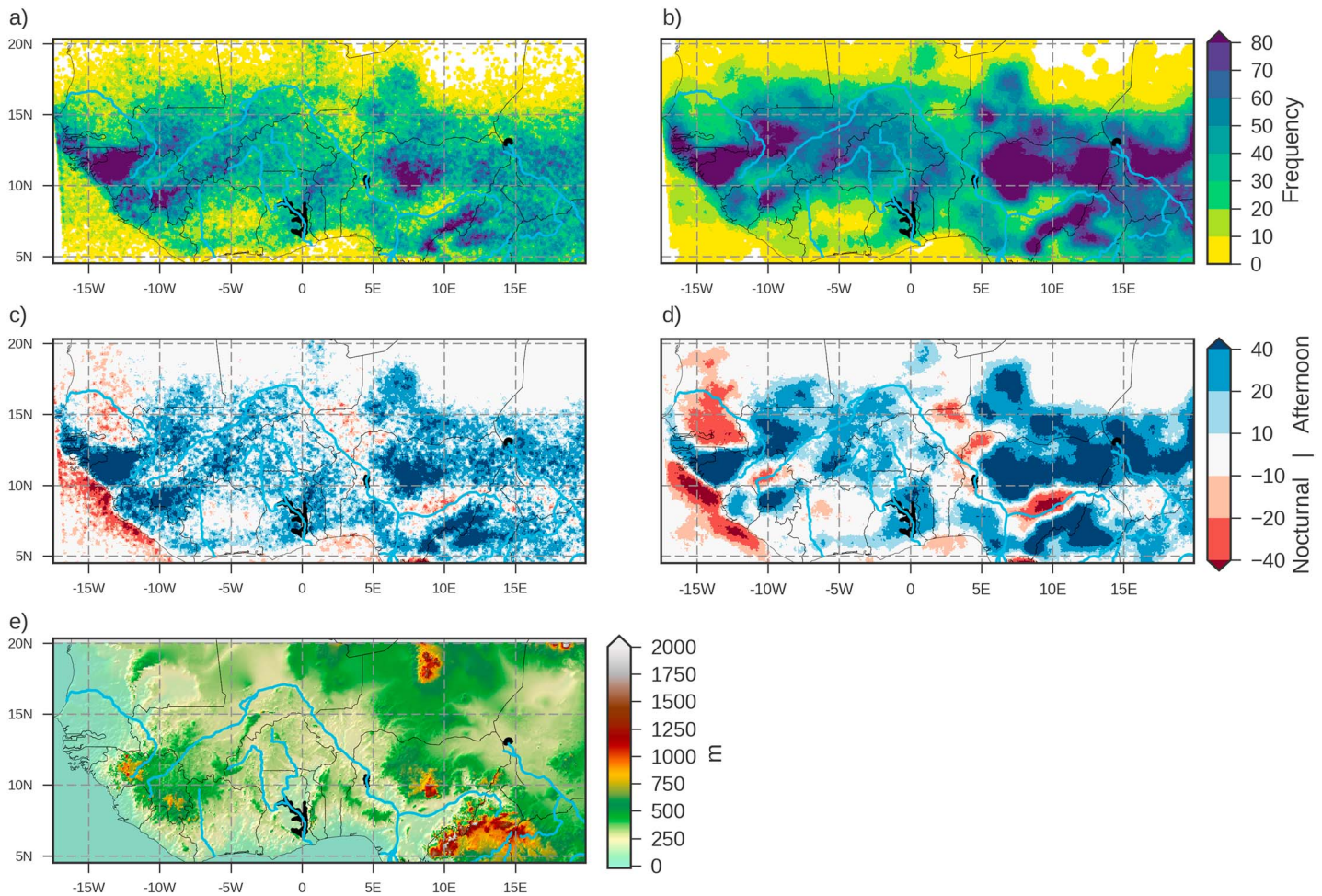


**Figure 11.** Maps for June–September 2004–2014 showing the frequency of subcloud features in the late afternoon (1800 UTC) for (a)  $\leq 35$  km and (b)  $\geq 80$  km and the difference in subcloud feature frequency between late afternoon and nighttime (1800 UTC to 0300 UTC) for (c)  $\leq 35$  km and (d)  $\geq 80$  km, irrespective of a Tropical Rainfall Measuring Mission overpass. The topography is shown in (e) for comparison.

The impact of applying a small-scale SCF filter is particularly beneficial in geographical regions where storms frequently produce very large, cold stratiform cloud shields, which are difficult to separate from cold convective features based on their temperature. Figure 9b suggests that information on the length scale of SCFs could significantly help to reduce this detection problem across the Sahel. Between 8 and 14°N, the average size of cold cloud systems exceeds 120,000 km<sup>2</sup>. Such systems typically comprise large stratiform areal fractions during the peak monsoon. Compared to the application of a temperature threshold of  $-80^{\circ}\text{C}$ , the probability for convective rain remains more stable over the meridional cross section when a small-scale threshold is applied.

### 5.3. Diurnal and Geographical Variability of Length Scales

The relative contribution to total rainfall associated with any length scale varies over the day depending on the respective development stages of MCSs. In Figure 10a, we show this relative contribution for each 2-hourly period of the day for SCFs on scales from 15 to 180 km. For small scales, the diurnal peak occurs in the afternoon (16–18 UTC). For SCFs greater than 80 km, maximum rainfall occurs in the evening and overnight (Figure 10b). This is consistent with the well-established life cycle of long-lived MCSs, which are triggered in the afternoon and reach their mature, fully grown phase with a developed stratiform anvil overnight before dissipating in the morning (Mathon and Laurent, 2001).

The diurnal cycles in Figures 10a and 10b can be interpreted in terms of variations in rainfall intensity and frequency per length scale. We find that the relative contribution to rainfall amounts is predominantly

determined by the frequency of SCFs at a given scale, that is, the number of pixels assigned to respective scales per 2-hourly bin (Figure 10c) rather than by a change in rainfall intensity (Figure 10d). On the contrary, the latter remains relatively constant throughout the day for each scale range: SCFs below 35 km show an average rainfall intensity of  $9 \text{ mm h}^{-1}$  as compared to considerably weaker  $4.5 \text{ mm h}^{-1}$  for SCFs larger than 60 km (Figure 10d).

Finally, we consider the spatial distribution of SCFs across the region, based on the analysis of all available MSG images for a given time of day, regardless of the availability of TRMM data (Figures 11a and 11b). In almost all regions, SCF frequencies are higher in the afternoon and early evening than in early morning (Figures 11c and 11d). This is consistent with the domain-mean late-afternoon peak in SCF frequency in Figure 10c. The frequency of afternoon SCFs shows clear maxima over elevated terrain. A weaker but distinct afternoon preference is also visible along the coastline, most likely linked to the sea breeze.

A dominance of nocturnal SCFs over land exists almost exclusively in regions devoid of, but downstream from, significant topographical features, in line with the findings of Zhang et al. (2016). Based on TRMM rainfall data across the region, they identified nocturnal rainfall peaks  $3^{\circ}$ – $10^{\circ}$  of longitude to the west of regions with afternoon rainfall maxima. The presence of these structures in Figure 11 suggests that our small-scale detection methodology may provide a useful tool in understanding how other, more subtle features, such as vegetation and soil moisture, also affect convective life cycles.

## 6. Discussion and Conclusion

Focusing on the West African region, this study has illustrated how wavelet-based scale decomposition can be used to derive a relationship between rainfall intensity and the length scales of cloud top temperatures of MCSs. By combining TRMM 2A25 surface rainfall with MSG thermal infrared images, we evaluated the potential in using length scale information in addition to cloud top temperatures for the identification of intensely precipitating areas within MCSs.

Starting at the storm scale, we showed that higher rainfall intensities are strongly coupled to colder cloud top temperatures; the probability for a storm to produce any extreme rainfall increases from less than 1.5% for minimum temperatures above  $-40^{\circ}\text{C}$  to over 80% when temperatures drop below  $-80^{\circ}\text{C}$ . At the same time, 90% of extreme rainfall occurrences over the study region are related to very large MCSs with a cloud area exceeding  $15,000 \text{ km}^2$ . For assessing the temperature-precipitation relationship at a subcloud scale, we therefore focused on 4,530 large MCSs below a temperature threshold of  $-40^{\circ}\text{C}$ . The scale decomposition was conducted for every single MCS using 2-D continuous wavelet analysis. This approach allowed us to identify individual subcloud features (SCFs) at different length scales. Compared to the cloud area at  $-40^{\circ}\text{C}$ , the defined SCFs encompass only 40% of the area while retaining 90% of all extreme rainfall pixels, and increasing the percentage of rainy pixels from 28.5% to 40.3%. This illustrates that, even without any further differentiation by scale or temperature, the method reduces the area of interest, that is, identifies cloud areas that are most likely to produce intense rain.

On average, we find extreme rainfall to be centered on such SCFs up to scales of about 60 km, illustrating that convective areas in the MCSs can be identified with this method. In accordance with the bulk analysis, the probability for convective rainfall in a specific region of the storm increases with locally colder cloud top temperatures. The most frequent occurrence of temperatures below  $-80^{\circ}\text{C}$  can be attributed to SCFs smaller than 35 km, coinciding with the highest probability for extreme rainfall compared to larger scales. Furthermore, the presented scale decomposition revealed a good performance in excluding cloud pixels that are most likely associated with stratiform cloud shields. These cloud shields can be cold but exhibit homogeneous features, which are assigned to larger scales. Consequently, the combination of temperature and scale information provided consistently higher probabilities for convective rainfall detection for scales below 35 km as compared to a temperature-only approach.

Furthermore, we were able to identify a mean growth in length scales over the diurnal cycle consistent with our knowledge of MCS life cycles. Interestingly, the average rainfall intensity for three different length scale ranges remains relatively constant over the day, with the smallest scales reaching  $8.8 \text{ mm h}^{-1}$ . This constant relationship between rainfall intensity and SCF length scale at different phases of the MCS life cycle is an appealing aspect of the approach, suggesting stable characteristics of the rainfall distribution per scale range.

However, the statistical relationship between cloud top temperature and rainfall intensity proved to be more robust for the initial bulk analysis at storm scale. At the subcloud (pixel) scale, the relationship is more chaotic. Even for cloud top temperatures below  $-80^{\circ}\text{C}$  embedded in small-scale features below 35 km, a combination that should be predestined for the extraction of convective cloud parts, only 33% of the pixels are indeed classified as convective in TRMM. However, it is worth to remember that the TRMM 2A25 product used here tends to underestimate convective rainfall amounts over land (e.g., Iguchi et al., 2009; Nesbitt et al., 2006; Rasmussen et al., 2013), which might reduce the actual correlation of cloud top temperatures and rainfall intensities. This implies that the method presented here would have to be refined if it were to be used for rainfall estimation techniques that aimed at combining temperature and scale information. Several approaches for addressing the large false alarm rate could be explored. A more restrictive design of the small-scale filtering could include a normalization of the wavelet power spectrum and using a common wavelet power threshold for all storms rather than the storm-relative approach used here. Another option might be the application of a pattern-matching algorithm to reduce the spatial offset that can occur between associated cloud top temperature and rainfall patterns. Generally, the wavelet scale decomposition leaves room for adjustment depending on the application and what kind of filtering is expected. In this sense, the definition of a “feature” and hence of identified scales within a continuous, heterogeneous field like cloud top temperature is not entirely objective.

Nevertheless, from a statistical point of view and given that the false alarm rate is a systematic bias, this method is a powerful approach for analyses of temporal or spatial changes in convective features, explicitly considering length scale dependencies, and could be a useful complement to more sophisticated OT detection algorithms. In addition, the dependence of a length scale approach on the relative structure of cloud top temperature rather than on absolute values is appealing when considering trends from different sensors, which can exhibit biases. Hence, the methodology can be applied as is to study trends at sub-MCS scales, following the findings of Taylor et al. (2017). It also allows us to look from a statistical perspective at feedbacks between MCSs and the land surface; brightness temperature data have been used before in West Africa to identify an important role of soil moisture heterogeneity in MCS initiation (Taylor et al., 2011). The small-scale detection method presented here will allow us to better understand surface feedbacks associated with organized convection. Other infrared imagers such as the Advanced Baseline Imager on the Geostationary Operational Environmental Satellites (Schmit et al., 2017) and the Advanced Himawari Imager (Bessho et al., 2016) would allow an extension of such analyses to other regions. Just like the Flexible Combined Imager on board the future Meteosat Third Generation (Durand et al., 2015), they provide information at a higher spatial resolution of 2 km, which could further improve the accurate localization of convective cores within MCSs.

Ultimately, our results demonstrate the basic suitability of 2-D wavelet scale decomposition for the analysis of subcloud structures and their relation to rainfall characteristics. This kind of scale analysis opens up a wide field of many further possible applications. Combining information on cloud top temperature and length scale, the presented method can help to identify changes in the properties of MCSs and associated rainfall over climatological time scales as well as for relatively small spatial scales.

#### Acknowledgments

The research leading to these results received funding from the UK's Natural Environment Research Council (NERC)/Department for International Development (DFID) Future Climate for Africa program, under the AMMA-2050 project (grant number NE/M020428/1), and from NERC funding of the VERA project (NE/M004295/1). We thank the providers of key data sets used here (EUMETSAT; NASA). MSG data are available from <http://www.eumetsat.int>, and data from the Tropical Rainfall Measuring Mission are available from <https://pmm.nasa.gov/>.

#### References

- Adler, R. F., & Negri, A. J. (1988). A satellite infrared technique to estimate tropical convective and stratiform rainfall. *Journal of Applied Meteorology*, 27(1), 30–51. [https://doi.org/10.1175/1520-0450\(1988\)027%3C0030:ASITTE%3E2.0.CO;2](https://doi.org/10.1175/1520-0450(1988)027%3C0030:ASITTE%3E2.0.CO;2)
- Ai, Y., Li, W., Meng, Z., & Li, J. (2016). Life cycle characteristics of MCSs in Middle East China tracked by geostationary satellite and precipitation estimates. *Monthly Weather Review*, 144(7), 2517–2530. <https://doi.org/10.1175/MWR-D-15-0197.1>
- Ai, Y., Li, J., Shi, W., Schmit, T. J., Cao, C., & Li, W. (2017). Deep convective cloud characterizations from both broadband imager and hyperspectral infrared sounder measurements. *Journal of Geophysical Research: Space Physics*, 122, 1700–1712. <https://doi.org/10.1002/2016JD025408>
- Alfaro, D. A., & Khairoutdinov, M. (2015). Thermodynamic constraints on the morphology of simulated midlatitude squall lines. *Journal of the Atmospheric Sciences*, 72, 3116–3137. <https://doi.org/10.1175/JAS-D-14-0295.1>
- Allen, M. R., & Ingram, W. J. (2002). Constraints on future changes in climate and the hydrologic cycle. *Nature*, 419(6903), 224–232. <https://doi.org/10.1038/nature01092>
- Antoine, J.-P. (2004). The 2-D wavelet transform, physical applications and generalizations. In J. C. Van den Berg (Ed.), *Wavelets in physics* (pp. 23–75). Cambridge: Cambridge University Press.
- Ashouri, H., Hsu, K., Sorooshian, S., Braithwaite, D. K., Knapp, K. R., Cecil, L. D., et al. (2015). PERSIANN-CDR: Daily precipitation climate data record from multi-satellite observations for hydrological and climate studies. *Bulletin of the American Meteorological Society*, 96(1), 69–83. <https://doi.org/10.1175/BAMS-D-13-00068.1>

- Awaka, J., Iguchi, T., Kumagai, H., & Okamoto, K. (1997). Rain type classification algorithm for TRMM precipitation radar. In *Proc. of the IEEE 1997 Intl. Geoscience and Remote Sensing Sym* (pp. 1633–1635). Singapore: IEEE.
- Bedka, K., & Khlopenkov, K. (2016). A probabilistic multispectral pattern recognition method for detection of overshooting cloud tops using passive satellite imager observations. *Journal of Applied Meteorology and Climatology*, 55(9), 1983–2005. <https://doi.org/10.1175/JAMC-D-15-0249.1>
- Berg, P., Moseley, C., & Haerter, J. O. (2013). Strong increase in convective precipitation in response to higher temperatures. *Nature Geoscience*, 6(3), 181–185. <https://doi.org/10.1038/ngeo1731>
- Bessho, K., Date, K., & Hayashi, M. (2016). An introduction to Himawari-8/9-Japan's new-generation geostationary meteorological satellites. *Journal of the Meteorological Society of Japan*, 94(2), 151–183. <https://doi.org/10.2151/jmsj.2016-009>
- Cheng, C., & Houze, R. A. (1979). The distribution of convective and mesoscale precipitation in GATE radar echo patterns. *Monthly Weather Review*, 107, 1370–1381.
- Corfidi, S. (2003). Cold pools and MCS propagation: Forecasting the motion of downwind-developing MCSs. *Weather and Forecasting*, 997–1017.
- Dee, D. P., Uppala, S. M., Simmons, A. J., Berrisford, P., Poli, P., Kobayashi, S., et al. (2011). The ERA-Interim reanalysis: Configuration and performance of the data assimilation system. *Quarterly Journal of the Royal Meteorological Society*, 137(656), 553–597. <https://doi.org/10.1002/qj.828>
- Durand, Y., Hallibert, P., Wilson, M., Lekouara, M., Grabarnik, S., Aminou, D., et al. (2015). The flexible combined imager onboard MTG: From design to calibration, Proc. SPIE 9639, Sensors, Systems, and Next-Generation Satellites XIX, 963903 (13 October 2015). <https://doi.org/10.1117/12.2196644>
- Dworak, R., Bedka, K., Brunner, J., & Feltz, W. (2012). Comparison between GOES-12 overshooting-top detections, WSR-88D radar reflectivity, and severe storm reports. *Weather and Forecasting*, 27(3), 684–699. <https://doi.org/10.1175/WAF-D-11-00070.1>
- Fink, A. H., & Reiner, A. (2003). Spatiotemporal variability of the relation between African Easterly Waves and West African Squall Lines in 1998 and 1999. *Journal of Geophysical Research*, 108(D11), 4332. <https://doi.org/10.1029/2002JD002816>
- Fiolleau, T., & Roca, R. (2013). Composite life cycle of tropical mesoscale convective systems from geostationary and low Earth orbit satellite observations: Method and sampling considerations. *Quarterly Journal of the Royal Meteorological Society*, 139(673), 941–953. <https://doi.org/10.1002/qj.2174>
- Froidevaux, P., Schlemmer, L., Schmidli, J., Langhans, W., & Schär, C. (2014). Influence of the background wind on the local soil moisture–precipitation feedback. *Journal of the Atmospheric Sciences*, 71(2), 782–799. <https://doi.org/10.1175/JAS-D-13-0180.1>
- Futyan, J. M., & Del Genio, A. D. (2007). Deep convective system evolution over Africa and the tropical Atlantic. *Journal of Climate*, 20(20), 5041–5060. <https://doi.org/10.1175/JCLI4297.1>
- Geerts, B., & Dejene, T. (2005). Regional and diurnal variability of the vertical structure of precipitation systems in Africa based on spaceborne radar data. *Journal of Climate*, 18(7), 893–916.
- Goldenberg, S. B., Houze, R. A. Jr., & Churchill, D. D. (1990). Convective and stratiform components of winter monsoon cloud cluster determined from geosynchronous infrared satellite data. *Journal of the Meteorological Society of Japan*, 68, 37–63.
- Gorman, P. A. O. (2015). Precipitation extremes under climate change. *Current Climate Change Reports*, 1(2), 49–59. <https://doi.org/10.1007/s40641-015-0009-3>
- Guy, N., & Rutledge, S. A. (2012). Regional comparison of West African convective characteristics: A TRMM-based climatology. *Quarterly Journal of the Royal Meteorological Society*, 138(666), 1179–1195.
- Hartley, A. J., Parker, D. J., Garcia-Carreras, L., & Webster, S. (2016). Simulation of vegetation feedbacks on local and regional scale precipitation in West Africa. *Agricultural and Forest Meteorology*, 222, 59–70. <https://doi.org/10.1016/j.agrformet.2016.03.001>
- Hodges, K. I., & Thorncroft, C. D. (1997). Distribution and statistics of African mesoscale convective weather systems based on the ISCCP Meteosat imagery. *Monthly Weather Review*, 125, 2821–2837.
- Houze, R. A. J. (2004). Mesoscale convective systems. *Reviews of Geophysics*, 42, RG4003. <https://doi.org/10.1029/2004RG000150>
- Houze, R. A., Rasmussen, K. L., Zuluaga, M. D., & Brodzik, S. R. (2015). The variable nature of convection in the tropics and subtropics: A legacy of 16 years of the Tropical Rainfall Measuring Mission satellite. *Reviews of Geophysics*, 53, 994–1021. <https://doi.org/10.1002/2015RG000488>
- Iguchi, T., Kozu, T., Kwiatkowski, J., Meneghini, R., Awaka, J., & Okamoto, K. (2009). Uncertainties in the rain profiling algorithm for the TRMM precipitation radar. *Journal of the Meteorological Society of Japan*, 87, 1–30.
- Joyce, R., & Arkin, P. A. (1997). Improved estimates of tropical and subtropical precipitation using the GOES precipitation index. *Journal of Atmospheric and Oceanic Technology*, 14(5), 997–1011. [https://doi.org/10.1175/1520-0426\(1997\)014%3C0997:IEOTAS%3E2.0.CO;2](https://doi.org/10.1175/1520-0426(1997)014%3C0997:IEOTAS%3E2.0.CO;2)
- Klein, C., Bliefenicht, J., Heinzeller, D., Gessner, U., Klein, I., & Kunstmann, H. (2017). Feedback of observed interannual vegetation change: A regional climate model analysis for the West African monsoon. *Climate Dynamics*, 48, 2837–2858. <https://doi.org/10.1007/s00382-016-3237-x>
- Kohler, M., Kalthoff, N., & Kottmeier, C. (2010). The impact of soil moisture modifications on CBL characteristics in West Africa: A case-study from the AMMA campaign. *Quarterly Journal of the Royal Meteorological Society*, 136(51), 442–455. <https://doi.org/10.1002/qj.430>
- Laurent, H., D'Amato, N., & Lebel, T. (1998). How important is the contribution of the mesoscale convective complexes to the Sahelian rainfall? *Physics and Chemistry of the Earth*, 23(5–6), 629–633. [https://doi.org/10.1016/S0079-1946\(98\)00099-8](https://doi.org/10.1016/S0079-1946(98)00099-8)
- Lauwaet, D., van Lipzig, N. P. M., & De Ridder, K. (2009). The effect of vegetation changes on precipitation and Mesoscale Convective Systems in the Sahel. *Climate Dynamics*, 33(4), 521–534. <https://doi.org/10.1007/s00382-009-0539-2>
- Lenderink, G., Barbero, R., Loriaux, J. M., & Fowler, H. J. (2017). Super Clausius-Clapeyron scaling of extreme hourly convective precipitation and its relation to large-scale atmospheric conditions. *Journal of Climate*, 30(15), 6037–6052. <https://doi.org/10.1175/JCLI-D-16-0808.1>
- Liu, C., & Zipser, E. J. (2009). “Warm rain” in the tropics: Seasonal and regional distributions based on 9 yr of TRMM data. *Journal of Climate*, 22(3), 767–779. <https://doi.org/10.1175/2008JCLI2641.1>
- Mahani, S. E., Gao, X., Sorooshian, S., & Imam, B. (2000). Estimating cloud top height and spatial displacement from scan-synchronous GOES images using simplified IR-based stereoscopic analysis. *Journal of Geophysical Research*, 105(D12), 15,597–15,608. <https://doi.org/10.1029/2000JD900064>
- Mahrooghly, M., Anantharaj, V. G., Younan, N. H., Aanstoos, J., & Hsu, K.-L. (2012). On an enhanced PERSIANN-CCS algorithm for precipitation estimation. *Journal of Atmospheric and Oceanic Technology*, 29, 922–932. <https://doi.org/10.1175/JTECH-D-11-00146.1>
- Maidment, R. I., Grimes, D., Allan, R. P., Tarnavsky, E., Stringer, M., Hewison, T., et al. (2014). The 30 year TAMSAT African Rainfall Climatology and Time series (TARCAT) data set. *Journal of Geophysical Research: Atmospheres*, 119, 10,619–10,644. <https://doi.org/10.1002/2014JD021927>
- Maidment, R. I., Grimes, D., Black, E., Tarnavsky, E., Young, M., Greatrex, H., et al. (2017). A new, long-term daily satellite-based rainfall dataset for operational monitoring in Africa. *Scientific Data*, 4, 170063. <https://doi.org/10.1038/sdata.2017.63>

- Marr, D., & Hildreth, E. (1980). Theory of edge detection. *Proceedings of the Royal Society B: Biological Sciences*, 207(1167), 187–217. <https://doi.org/10.1098/rspb.1980.0020>
- Mathon, V., Laurent, H., & Lebel, T. (2002). Mesoscale convective system rainfall in the Sahel. *Journal of Applied Meteorology*, 41(11), 1081–1092. [https://doi.org/10.1175/1520-0450\(2002\)041%3C1081:MCSRIT%3E2.0.CO;2](https://doi.org/10.1175/1520-0450(2002)041%3C1081:MCSRIT%3E2.0.CO;2)
- Mathon, V., & Laurent, H. (2001). Life cycle of Sahelian mesoscale convective cloud systems. *Quarterly Journal of the Royal Meteorological Society*, 127, 377–406.
- Mohr, K. I. (2004). Interannual, monthly, and regional variability in the wet season diurnal cycle of precipitation in sub-Saharan Africa. *Journal of Climate*, 17(12), 2441–2453. [https://doi.org/10.1175/1520-0442\(2004\)017%3C2441:IMARV%3E2.0.CO;2](https://doi.org/10.1175/1520-0442(2004)017%3C2441:IMARV%3E2.0.CO;2)
- Mohr, K. I., & Thorncroft, C. D. (2006). Intense convective systems in West Africa and their relationship to the African easterly jet. *Quarterly Journal of the Royal Meteorological Society*, 132(614), 163–176. <https://doi.org/10.1256/qj.05.55>
- Nesbitt, S. W., Cifelli, R., & Rutledge, S. A. (2006). Storm morphology and rainfall characteristics of TRMM precipitation features. *Monthly Weather Review*, 134, 2702–2721.
- Parker, M. D., & Johnson, R. H. (2000). Organizational modes of midlatitude mesoscale convective systems. *Monthly Weather Review*, 128(10), 3413–3436. [https://doi.org/10.1175/1520-0493\(2001\)129%3C3413:OMOMMC%3E2.0.CO;2](https://doi.org/10.1175/1520-0493(2001)129%3C3413:OMOMMC%3E2.0.CO;2)
- Rasmussen, K. L., Choi, S. L., Zuluaga, M. D., & Houze, R. A. (2013). TRMM precipitation bias in extreme storms in South America. *Geophysical Research Letters*, 40, 3457–3461. <https://doi.org/10.1002/grl.50651>
- Raut, B. A., Karekar, R. N., & Puranik, D. M. (2009). Spatial distribution and diurnal variation of cumuloniform clouds during Indian Summer Monsoon. *Journal of Geophysical Research*, 114, 1–12. <https://doi.org/10.1029/2008JD011153>
- Roca, R., Aublanc, J., Chambon, P., Fiolleau, T., & Viltard, N. (2014). Robust observational quantification of the contribution of mesoscale convective systems to rainfall in the tropics. *Journal of Climate*, 27(13), 4952–4958. <https://doi.org/10.1175/JCLI-D-13-00628.1>
- Schmit, T. J., Griffith, P., Gunshor, M. M., Daniels, J. M., Goodman, S. J., & Lebar, W. J. (2017). A closer look at the ABI on the GOES-R series. *Bulletin of the American Meteorological Society*, 98(4), 681–698.
- Schumacher, C., & Houze, R. A. (2006). Stratiform precipitation production over sub-Saharan Africa and the tropical East Atlantic as observed by TRMM. *Quarterly Journal of the Royal Meteorological Society*, 132(620), 2235–2255.
- Sohn, B. J., Ryu, G.-H., Song, H.-J., & Ou, M.-L. (2013). Characteristic features of warm-type rain producing heavy rainfall over the Korean peninsula inferred from TRMM measurements. *Monthly Weather Review*, 141(11), 3873–3888. <https://doi.org/10.1175/MWR-D-13-00075.1>
- Taylor, C. M., Belušić, D., Guichard, F., Parker, D. J., Vischel, T., Bock, O., et al. (2017). Frequency of extreme Sahelian storms tripled since 1982 in satellite observations. *Nature*, 544(7651), 475–478. <https://doi.org/10.1038/nature22069>
- Taylor, C. M., Gounou, A., Guichard, F., Harris, P. P., Ellis, R. J., Couvreux, F., & Kauwe, M. D. (2011). Frequency of Sahelian storm initiation enhanced over mesoscale soil-moisture patterns. *Nature Geoscience*, 4(7), 430–433. <https://doi.org/10.1038/ngeo1173>
- Taylor, C. M., & Lebel, T. (1998). Observational evidence of persistent convective-scale rainfall patterns. *Monthly Weather Review*, 126, 1597–1607.
- Torrence, C., & Compo, G. P. (1998). A practical guide to wavelet analysis. *Bulletin of the American Meteorological Society*, 79(1), 61–78.
- Tropical Rainfall Measuring Mission (2011). TRMM precipitation radar rainfall rate and profile L2 1.5 hours V7, Greenbelt, MD: Goddard Earth Sciences Data and Information Services Center (GES DISC). Retrieved from [https://disc.gsfc.nasa.gov/datacollection/TRMM\\_2A25\\_7.html](https://disc.gsfc.nasa.gov/datacollection/TRMM_2A25_7.html), Accessed 10.01.2018
- Vicente, G. A., Scofield, R. A., & Menzel, W. P. (1998). The operational GOES infrared rainfall estimation technique. *Bulletin of the American Meteorological Society*, 79(9), 1883–1893. [https://doi.org/10.1175/1520-0477\(1998\)079%3C1883:TOGIRE%3E2.0.CO;2](https://doi.org/10.1175/1520-0477(1998)079%3C1883:TOGIRE%3E2.0.CO;2)
- Wang, N., & Lu, C. (2010). Two-dimensional continuous wavelet analysis and its application to meteorological data. *Journal of Atmospheric and Oceanic Technology*, 27(4), 652–666. <https://doi.org/10.1175/2009JTECHA1338.1>
- Weniger, M., Kapp, F., & Friederichs, P. (2017). Spatial verification using wavelet transforms: A review. *Quarterly Journal of the Royal Meteorological Society*, 143, 120–136. <https://doi.org/10.1002/qj.2881>
- Wolters, E. L. A., & Roebeling, R. A. (2011). Evaluation of rainfall retrievals from SEVIRI reflectances over West Africa using TRMM-PR and CMORPH. *Hydrology and Earth System Sciences*, 15, 437–451. <https://doi.org/10.5194/hess-15-437-2011>
- Wu, P., Christidis, N., & Stott, P. (2013). Anthropogenic impact on Earth's hydrological cycle. *Nature Climate Change*, 3, 807–810.
- Xu, W., & Zipser, E. J. (2012). Properties of deep convection in tropical continental, monsoon, and oceanic rainfall regimes. *Geophysical Research Letters*, 39, L07802. <https://doi.org/10.1029/2012GL051242>
- Yano, J., & Jakubiak, B. (2016). Wavelet-based verification of the quantitative precipitation forecast. *Dynamics of Atmospheres and Oceans*, 74, 14–29. <https://doi.org/10.1016/j.dynatmoce.2016.02.001>
- Zhang, G., Cook, K. H., & Vizy, E. K. (2016). The diurnal cycle of warm season rainfall over West Africa. Part I: Observational analysis. *Journal of Climate*, 29(23), 8423–8437. <https://doi.org/10.1175/JCLI-D-15-0874.1>